

# 1 **Space-Time Localization of Inner Heliospheric Plasma Turbulence Using** 2 **Multiple Spacecraft Radio Links**

3

4 Adam C. Richie-Halford  
5 Los Angeles Air Force Base, El Segundo, CA 90245

6

7 L. Iess  
8 Dipartimento di Ingegneria Aerospaziale e Astronautica, Università di Roma “La Sapienza,”  
9 I-00184 Roma, Italy

10

11 P. Tortora  
12 DIEM -- II Facoltà di Ingegneria, Università di Bologna, I-47110 Forlì, Italy

13

14 J. W. Armstrong, S. W. Asmar, Richard Woo  
15 Jet Propulsion Laboratory, California Institute of Technology, Pasadena CA 91109

16

17 Shadia Rifai Habbal  
18 Institute of Astronomy, University of Hawaii

19

20 Huw Morgan  
21 Institute of Astronomy, University of Hawaii, and Aberystwyth University, Wales, UK

22

23

24

25

26

27

## 28 **Abstract**

29

30 Radio remote sensing of the heliosphere using spacecraft radio signals has been used to study the  
31 near-sun plasma in and out of the ecliptic, close to the sun, and on spatial and temporal scales not  
32 accessible with other techniques. Studies of space-time variations in the inner solar wind are  
33 particularly timely because of the desire to understand and predict space weather, which can  
34 disturb satellites and systems at 1AU and affect human space exploration. Here we demonstrate  
35 proof-of-concept of a new radio science application for spacecraft radio science links. The  
36 differing transfer functions of plasma irregularities to spacecraft radio up- and downlinks can be  
37 exploited to localize plasma scattering along the line of sight. We demonstrate the utility of this  
38 idea using Cassini radio data taken in 2001-2002. Under favorable circumstances we  
39 demonstrate how this technique, unlike other remote sensing methods, can determine center-of-  
40 scattering position to within a few thousandths of an AU and thickness of scattering region to  
41 less than about 0.02 AU. This method, applied to large data sets and used in conjunction with  
42 other solar remote sensing data such as white light data, has space weather application in studies  
43 of inhomogeneity and nonstationarity in the near-sun solar wind.

44

45

## 46 1. Introduction

47

48 Radio links to and from deep space probes are used for spacecraft command and control,  
49 telemetry, navigation, and radio science. Radio science applications include determination of  
50 planetary and satellite gravitational fields, measurements of properties of planetary atmospheres,  
51 ionospheres, and rings, studies of the solar wind, solar system tests of relativistic gravity, and  
52 searches for low-frequency gravitational radiation [e.g., *Tyler et al. 2001*, *Kliore et al. 2004*]. In  
53 addition to probing otherwise inaccessible regions of the solar system, the link signal-to-noise  
54 ratios (SNRs) and instrumental frequency stability are often excellent and allow sensitive  
55 propagation measurements [*Asmar et al. 2005*]. For heliospheric plasma investigations, radio  
56 propagation observations have been used to study the solar wind plasma over a wide range of  
57 distances from the sun, in- and out-of-the-ecliptic, and on spatial and temporal scales which  
58 cannot be measured with other techniques.

59

60 The high SNR and excellent time resolution of radio data lend themselves to studies of  
61 nonstationarity and inhomogeneity of the inner heliospheric plasma. Interest in space-time  
62 variations in the inner solar wind has been invigorated by the desire to understand and predict  
63 (via propagation or co-rotation) space weather, which can disturb satellites and systems at the  
64 earth, affect human space exploration, and (via intensity and phase scintillation) cause significant  
65 disruption of deep space telecommunications [*Woo 2007* and references therein]. In this paper  
66 we present a new technique, based on processing of multiple simultaneous radio links to and  
67 from a spacecraft, for space-time localization of inner heliospheric plasma disturbances.

68

69

## 70 2. Transfer Functions of Plasma Irregularities to Doppler Links

71

72 At microwave frequencies solar-wind-induced refractive index variations are  $\delta n_e(\mathbf{r}) =$   
73  $-\lambda^2 r_e \delta n_e(\mathbf{r}) / (2\pi)$ , where  $\lambda$  is the radio wavelength,  $r_e$  is the classical electron radius, and  $\delta n_e$  is  
74 the electron density fluctuation at three-dimension position vector,  $\mathbf{r}$ . A monochromatic wave  
75 propagating through a thin scattering region (“screen”) having thickness  $\Delta z$  develops a  
76 geometrical optics phase shift  $(2\pi/\lambda) \delta n_e(\mathbf{r}) \Delta z$ . This phase shift is the same for a wave

77 propagating either “up” or “down” through the screen at point  $\mathbf{r}$ . This attribute can be used for  
78 space-time localization of plasma irregularities.

79

80         Although the application to plasma localization given here is new, the idea was originally  
81 used in noise budget analysis of precision Doppler tracking experiments [*Estabrook & Wahlquist*  
82 1975, *Estabrook* 1978, *Vessot & Levine* 1978]. The transfer function of plasma irregularities to  
83 the observed time series depends on the tracking mode. When spacecraft observations are in the  
84 two-way mode (downlink radio signal phase-locked to an uplink radio transmission) plasma  
85 fluctuations have a “two-pulse” response in the Doppler frequency time series [*Estabrook &*  
86 *Wahlquist* 1975, *Estabrook* 1978]. This is illustrated in Figure 1. The upper plot is a space-time  
87 diagram, showing the ground station continuously transmitting a signal to the spacecraft and  
88 continuously receiving a signal from that spacecraft. Suppose that the radio center frequencies  
89 of the up- and downlink signals are the same. In the two-way mode, the Doppler time series  $y_2(t)$   
90 is the difference between the frequency of the received downlink signal and the frequency of a  
91 ground reference oscillator. For two-way observations the ground reference oscillator also  
92 provided the signal transmitted to the spacecraft a two-way light time,  $T_2$ , earlier. A localized  
93 plasma blob at distance  $x$  along the line-of-sight perturbs the phase on both the up- and  
94 downlink, as illustrated, giving rise to two events in the two-way tracking time series separated  
95 by a time lag depending on the earth-blob distance:  $T_2 - 2x/c$ .

96

97         Comparison of two-way and downlink plasma time series have been used to localize a  
98 dominant plasma screen [e. g., *Armstrong* 2006]. In some tracking situations, however, more  
99 information is available. The data analyzed here were taken with the five-link Cassini radio  
100 system [*Kliore et al.* 2004]. With this radio configuration the plasma contribution to the up- and  
101 downlinks,  $y_{up}(t)$  and  $y_{dn}(t)$ , can be computed separately [*Jess et al.* 2003, *Bertotti et al.* 2003,  
102 *Tortora et al.* 2004]. The times series  $y_{up}(t)$  and  $y_{dn}(t)$  respond to a localized plasma blob with  
103 one event in each time series. These events are also separated in time by  $T_2 - 2x/c$  (lower panels  
104 in Figure 1). By cross correlating the up- and downlink Doppler time series the time separation  
105 of the plasma events can be measured and hence the plasma blob’s distance from the earth  
106 determined. Since the plane-of-sky position is known (we point the ground antenna at the  
107 accurately-known spacecraft position), this technique allows localization of plasma events in  
108 time and three space dimensions.

109 In the idealized case of a geometrically thin screen, the uplink and downlink beams cross  
110 the thin screen at exactly one point, the phase shifts of up- and downlink are exactly the same,  
111 and the time series of up and downlink Doppler are exact, temporally offset, copies. The value  
112 of the up- and downlink Doppler cross correlation function is then unity at the correct  
113  $T_2 - 2x/c$  lag. If the screen has finite thickness, different space-time line segments contribute to  
114 the up- and downlinks. Since the line segments traversed by the up- and downlinks in the thick  
115 screen case do not exactly overlap in space-time, the up- and downlink times series are no longer  
116 offset copies of each other and peak crosscorrelation values will be less than unity. The  
117 crosscorrelation function's (ccf's) difference from unity can be used to bound the thickness of a  
118 screen dominating the observed Doppler scintillation, as discussed in the Appendix.

119

120

### 121 **3. Observations and Signal Processing**

122

123 The data used in this proof-of-concept study are from superior conjunctions tracks in  
124 2001 and 2002 taken for the Cassini relativity experiment [*Tortora et al. 2002, Bertotti et al.*  
125 2003]. During these solar conjunction intervals (+/- 15 days from conjunction during 2002) the  
126 spacecraft was several astronomical units from the earth. The observations used the full 5-link  
127 Cassini radio system [*Kliore et al. 2000, Bertotti et al. 2003*]: X-band downlink ( $\approx 8.4$  GHz)  
128 coherent with X-band uplink ( $\approx 7.2$  GHz), Ka-band downlink ( $\approx 32$  GHz) coherent with Ka-band  
129 uplink ( $\approx 34$  GHz), and a Ka-band downlink coherent with the X-band uplink. All data used  
130 here were taken with the NASA/JPL Deep Space Network 34-meter tracking antenna DSS25.  
131 The 5-link data allow plasma contributions to the Doppler, referenced here to X-band, to be  
132 separately computed for the up- and downlinks [*Tortora et al. 2003*]. In this initial study we  
133 band-pass filtered  $y_{\text{up}}(t)$  and  $y_{\text{dn}}(t)$  separately using arbitrary-but-reasonable band edge  
134 frequencies of 0.00056 and 0.02 Hz. This filtering, the intrinsically large SNRs of the Cassini  
135 links, and the excellent frequency stability of the ground and spacecraft systems allowed accurate  
136 estimation of the plasma contribution: the rms plasma signal is more than 300 times larger than  
137 the rms non-plasma estimation error 'noise' in the data shown here.

138

139 To implement the method we computed the cross-correlation function (ccf) between  
140  $y_{\text{up}}(t)$  and  $y_{\text{dn}}(t')$  as follows. Time series  $y_{\text{dn}}(t')$  was multiplied by a triangular time window,

141  $\Lambda((t - t') / 1800 \text{ seconds}))$ , centered on reference downlink time,  $t$ . (Here  $\Lambda(t) = 0$  if  $|t| > 1$  and  
142  $1 - |t|$  if  $|t| < 1$ .) Similarly  $y_{\text{up}}(t')$  was windowed with  $\Lambda((t - t' - T_2 + 1000 \text{ seconds}) / 1800$   
143 seconds). The 1000 second offset was chosen because of the *a priori* expectation that the main  
144 contribution would be near 1 AU from the earth ( $1 \text{ AU} / \text{speed of light} \approx 500 \text{ seconds}$ ). These  
145 windowed time series were crosscorrelated, giving the cross correlation function as a function of  
146 time lag,  $\tau$ , and reference downlink time,  $t$ . Time lag was converted to line of sight range,  $x$ :  $\tau =$   
147  $T_2 - 2x/c$ . The triangular time windows were then advanced by 10 seconds for each of the up-  
148 and down link time series and the process repeated. This gave the plasma-contribution ccf as a  
149 function of distance along the line of sight and time throughout the tracking pass.

150  
151

#### 152 4. Examples and Discussion

153

154 Figure 2 shows the band-pass-filtered up- and downlink plasma-contribution time series  
155 for a tracking pass on 2001 May 29 (day-of-year, DOY, 149; sun-earth-spacecraft angle  $\approx 6.6$   
156 degrees;  $T_2 \approx 6825$  seconds, varying by  $\approx 2$  seconds over the pass.). The data show clear  
157 temporal nonstationarity, with higher variability at the start and end of the pass and lower  
158 variability in the middle of the pass. Even by eye, there is clear positive correlation between the  
159 up- and downlink time series, including several high SNR discrete ‘events’ (e.g. near 1730 UT,  
160 2230 UT, and 2300 UT in the downlink, with corresponding events  $\sim T_2 - 1000$  seconds later in  
161 the uplink).

162

163 Figure 3 shows the space-time correlation function for these 2001 DOY 149 data. We  
164 plot contours down to 0.4 (pilot studies cross correlating these time series with zero time lag  
165 between them suggested correlations up to about 0.3 could occur by chance.) Figure 3 has two  
166 principal features. First, there is high correlation – greater than 0.95 near 1730 UT and peaking  
167 at  $\approx 0.99$ , e.g., for identifiable events near 2200-2300 UT -- over much of the track. Second, the  
168 lags where the correlation function peaks indicate plasma disturbances mostly located  
169 systematically farther away than the raypath’s closest approach point to the sun at  $\approx 1 \text{ AU} \cos(6.6$   
170 degrees) = 0.99 AU. The regions where the correlation is high (e.g.  $> 0.9$ ) give upper bounds on  
171 the effective screen thickness (see Appendix). Simulations of Kolmogorov turbulence in a  
172 uniform-thickness screen at 1 AU (and with the same signal processing used for the actual time

173 series) give, as expected, correlation of unity when the screen is geometrically thin. Increasing  
174 the full-width screen thickness to  $\approx 0.05$  AU gives peak correlation  $\approx 0.9$ . Thus, for the signal  
175 processing parameters in this pilot analysis, we estimate the full-width scattering region  
176 thickness in the high-correlation ( $>0.9$ ) intervals of Figure 3 to be less than or  $\approx 0.05$  AU = 7.5  
177 million km. During some parts of the 2001 DOY 149 track the screen thickness appears to be  
178 smaller than 0.05 AU. The region between  $\approx 2210$ -2320 UT, for example, has very high  
179 correlation (greater than 0.97) and a perhaps slightly trending range (as determined from the lag  
180 of the ccf's peak) from about 1.025 AU near 2210 UT to about 1.03 AU near 2320 UT. The  $>$   
181 0.97 correlation suggests, from the finite-thickness screen simulations, that the full width of the  
182 region dominating the plasma scattering is less than  $\approx 0.02$  AU over this entire time interval. We  
183 also can estimate the accuracy of the fiducial range from the up- and downlink cross spectrum,  
184 under the assumption that there is a unique range-to-screen over this interval (see Appendix).  
185 For this highly-correlated interval the range is particularly well-determined:  $1.028 \pm 0.003$  AU.

186

187 We looked at coronal images to see if there is an obvious plane-of-sky counterpart for  
188 these disturbances on 2001 DOY 149. These disturbances could be associated with the line of  
189 sight crossing the (mainly face-on) heliospheric current sheet (HCS) in the inner corona [*Woo et*  
190 *al.* 1995]; the relevant scattering region may be associated with disturbances in and around the  
191 heliospheric plasma sheet (HPS) which surrounds the HCS [*Winterhalter et al.* 1994]. Figure 4  
192 shows a map of the coronal density structure at a height of 4 solar radii (Rs) for Carrington  
193 Rotation 1976, calculated using a solar rotational tomography technique [*Morgan et al.* 2009]  
194 from  $\sim 2$  weeks of the LASCO/SOHO C2 [*Brueckner et al.* 1995] coronagraph observations.  
195 Red is high density, black is low. The x-axis refers to Carrington rotation longitude (CRL), the  
196 y-axis to solar latitude. During 2001 May 29, the meridional CRL (along the Earth-Sun line) is  
197 54 degrees. The point along the Earth-Cassini line of sight closest to the sun is at CRL 324  
198 degrees. This point is shown as a diamond on the map. The three dotted and dashed lines are the  
199 position of the HCS, calculated using a potential field source surface (PFSS) extrapolation of  
200 photospheric magnetic field observations made by the Wilcox Solar Observatory [*Altschuler*  
201 *and Newkirk* 1969, *Schatten et al.* 1969, *Wang and Sheeley* 1992]. The three lines give different  
202 positions of the HCS when different boundary conditions are applied. The reasonable agreement  
203 between the PFSS and tomography results at mid-to-high latitudes show that the estimate of the  
204 HCS position is fairly accurate (PFSS is not always accurate at times outside solar minimum: see

205 *Morgan and Habbal* [2007]), therefore the subsolar point along the Earth-Cassini line of sight  
206 must be close to the HCS during 2001 May 29. (For various reasons, the tomography method  
207 fails near the equator, so should not be trusted there.) The thicknesses of the HCS and HPS vary  
208 by an order of magnitude as observed by spacecraft at 1 and 5AU [*Winterhalter et al.* 1994,  
209 *Smith* 2001, Zhou et al 2005]. We note that our approximate upper bound of 0.02 AU for the  
210 thickness of the 2001 DOY 149 near-sun scattering region is consistent with (about a factor of 2  
211 larger than) the largest HPS thickness observed at 1 AU, but much larger than the  $\sim 0.001$  AU  
212 median HPS thickness at 1AU [*Winterhalter et al.* 1994, Zhou et al. 2005].

213  
214 The data in Figures 2-3 show a relatively simple case of well-localized, dominant  
215 scattering and are exemplary of the method. The technique is also diagnostic in more  
216 complicated situations. Figure 5 shows the ccf for 2002 DOY 160 (= 2002 June 9; sun-earth-  
217 spacecraft angle  $\approx 9.5$  degrees;  $T_2 \approx 8365$  seconds.) In contrast with 2001 DOY 149, the  
218 correlation levels are lower, indicative of less-well-localized scattering on this day Especially  
219 during the middle part of this track, the correlation is comparable to or below the contouring  
220 threshold (0.4), indicating substantially extended scattering along the line-of-sight. Indeed we  
221 have data from tracks where the scintillation level, as evidenced from the rms Doppler  
222 fluctuation, is substantial but the contribution is poorly localized over an entire  $\sim 8$  hour tracking  
223 pass.

224  
225 Finally, the technique is still in development and our current understanding of its  
226 strengths and limitations is not complete. It is, however, clear that localization will not work  
227 well when the temporal duration of a plasma fluctuation is long compared with the earth-  
228 spacecraft light time. In this limit, the width of the Doppler disturbances on the up and  
229 downlinks overlap and signature is lost. (This is not a practical problem for space weather  
230 studies.) We have done preliminary studies of the inversion of idealized thick-screen scattering  
231 distributions. In suitable situations the square of the Fourier transform of the scattering  
232 distribution along the line of sight multiplies the up- and downlink squared coherency spectrum.  
233 Using this, one could recover a measure of an extended medium's line-of-sight spatial  
234 distribution. Finally, we have not yet experimented with pre-filtering of the data. In this pilot  
235 study we chose a reasonable passband to demonstrate the method clearly but no attempt was

236 made at optimization. By looking at a different region of the fluctuation spectrum, or by  
237 prewhitening the times series, we may be able to improve resolution.

238

239

## 240 **5. Summary**

241

242 This paper gave a proof-of-concept demonstration of a technique to localize inner  
243 heliospheric plasma disturbances in space and time. The method is based on the differing  
244 transfer functions of plasma scintillation to one- and two-way radio links between the earth and a  
245 distant spacecraft. In the technique's simplest form, discussed here, the up- and downlink  
246 plasma time series are compared to localize dominant plasma irregularities in time and along the  
247 line-of-sight. Examples were shown for a situation where the scattering is dominated by a thin  
248 screen at well-defined location (Figure 3) and a situation where the scattering is more extended  
249 (Figure 5). When combined with other remote sensing observations such as white light images  
250 (and other simultaneous radio observations--e.g. intensity scintillation), this method has  
251 application in studies of inhomogeneity, nonstationarity, and other manifestations of inner  
252 heliospheric plasma variability.

253

254

255

256 *Acknowledgements:* We have greatly benefited from discussions with Frank B. Estabrook about  
257 the method. We thank W. A. Coles, B. J. Rickett, S. R. Spangler, and an anonymous referee for  
258 comments on the paper. ARH's work was performed at the Jet Propulsion Laboratory while on a  
259 US Air Force-JPL employee exchange program. LI and PT were supported in part by the Italian  
260 Space Agency (ASI). SH's and HM's research was supported by NASA grant NNX07AH90G  
261 to the University of Hawaii. For JWA, SWA and RW the research described here was carried  
262 out at the Jet Propulsion Laboratory, California Institute of Technology, under a contract with the  
263 National Aeronautics and Space Administration. We also thank the personnel of the Cassini  
264 Project, the JPL Radio Science Systems Group, and the NASA/JPL Deep Space Network. The  
265 SOHO/LASCO data used here are produced by a consortium of the Naval Research Laboratory  
266 (USA), Max-Planck-Institut fur Aeronomie (Germany), Laboratoire d'Astronomie (France), and  
267 the University of Birmingham (UK). SOHO is a project of international cooperation between



268 ESA and NASA. The Wilcox Solar Observatory's photospheric field data and extrapolations  
269 were obtained from the WSO section of Stanford University's website courtesy of J. T.  
270 Hoeksema. WSO is supported by NASA, the NSF, and ONR.  
271

272 **Appendix:** Distance Uncertainty and Screen Thickness Estimate

273

274 The accuracy of the ccf time lag, hence the accuracy of the range to a plasma screen, can  
275 be estimated from the cross spectrum of the up- and downlink time series. Assume there is a thin  
276 screen (justified empirically in cases where the peak correlation of the ccf is close to unity),  
277 hence a unique distance of the plasma disturbances from earth. Then there is a unique time lag  
278 in the ccf associated with that screen: the up- and downlink time series are copies of themselves  
279 offset by  $\tau_{\text{true}} = T_2 - 2x/c$ . In real situations approximating this idealization (e.g. the data  
280 between  $\approx 2210$ - $2320$  on 2001 DOY 149), the lag will be nonunique due to variability of the true  
281 range over the time interval, finite thickness of the “screen”, and estimation error of the ccf. This  
282 nonuniqueness reflects itself in range uncertainty.

283

284 We can estimate range accuracy from the statistics of the cross-spectral phase estimates  
285 [*Jenkins and Watts* 1969]. The idea is to pre-align the two time series,  $y_{\text{up}}$  and  $y_{\text{dn}}$  by an initial  
286 estimate of the true offset,  $\tau^*$ , determined for example from the peak of the average ccf over the  
287 time interval. This initial lag estimate will in general have an error:  $\tau^* = \tau_{\text{true}} + \delta\tau$ . If  $\delta\tau$  is non-  
288 zero then, from the shift theorem for Fourier transforms [*Bracewell* 1965], there will be a non-  
289 zero slope in the cross spectral phase (=inverse tangent of  $\text{Im}[C(f)]/\text{Re}[C(f)]$ , where  $C(f)$  is the  
290 cross-spectrum). The numerical value of the slope will be  $2\pi\delta\tau$ , from which the correction  $\delta\tau$   
291 can be estimated. The uncertainty in the final best-fit lag can then be determined from the  
292 uncertainty in the slope of the cross-spectral phase.

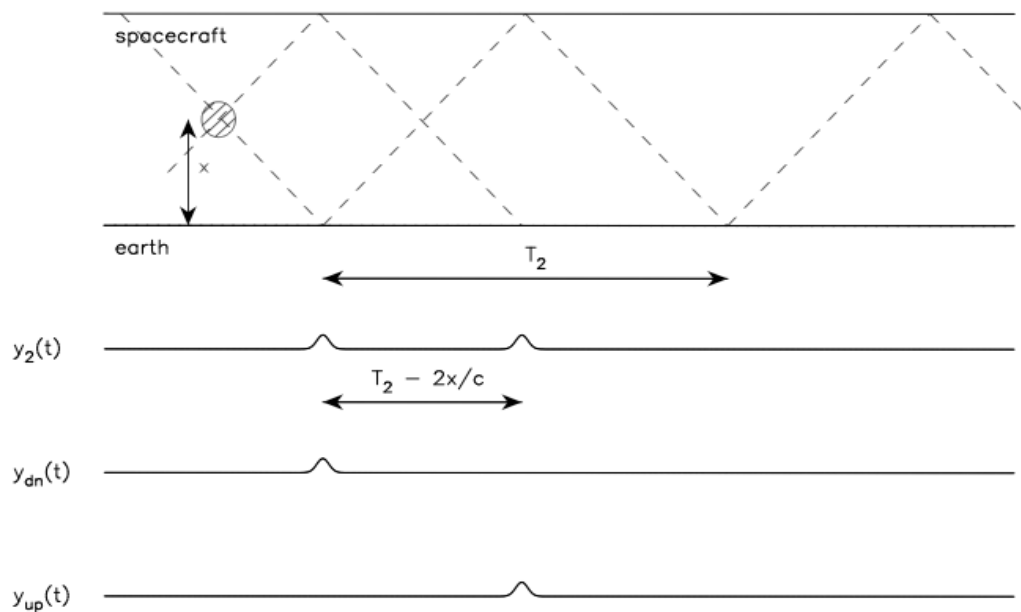
293

294 Consider the downlink data during the received time interval 2210-2320 UT and its  
295 uplink counterpart in the interval  $\sim T_2$ -1000 seconds later. Based on the ccf in this time interval,  
296 the uplink time series was pre-aligned relative to the downlink by  $\tau^* = 5796$  seconds. The  
297 smoothed auto spectra and smoothed cross spectrum were estimated in three separate procedures  
298 by Fourier transforming blocks of data 1024, 512, and 256 seconds long, giving 4+, 8+, and 16+  
299 averages during the 2210-2320 UT time interval. Rectangular transform windows were used,  
300 giving frequency resolution of 1/1024sec, 1/512sec, and 1/256 sec, respectively. Smoothing was  
301 done via simple averages of the Fourier transform-squared (for the auto spectra) and separate  
302 averages of the real and imaginary parts of the cross spectrum. The smoothed squared-

303 coherency,  $\kappa_{12}^2(f)$ , was estimated by forming the modulus-squared of the cross spectrum divided  
304 by the product of the auto spectra [Jenkins and Watts 1969]. The smoothed cross-spectral phase,  
305  $\phi_{12}(f)$ , was computed from the inverse tangent of the ratio of the smoothed imaginary part of the  
306 cross spectrum to the smoothed real part. Figure A1 shows these quantities for the three  
307 frequency resolutions. The slope of the cross-spectral phase in the Fourier band 0-0.01 Hz, after  
308 alignment by 5796 seconds, is non-zero and indicates an additional offset of 0.1 sec would be  
309 required for best alignment. The formal standard deviation in the slope of the cross-spectral  
310 phase is small (corresponding to a standard deviation in the estimated best-lag of less than 1  
311 second). The error in the slope is poorly estimated, however, due in part to the small number of  
312 points going into its determination. Instead of using the formal standard deviation in the slope,  
313 we adopt a more conservative viewpoint: the uncertainty in the slope of the residual cross  
314 spectral phase in Figure A1 appears bounded by +/- 10 degrees/0.01 Hz. This gives an  
315 uncertainty in the 5796.1 second time lag estimate of < 2.8 seconds and hence a formal  
316 uncertainty in the distance (for this high-correlation interval, not for a typical interval) of less  
317 than 0.003 AU.

318

319 A finite-thickness screen will not have unity cross-correlation because the up- and  
320 downlink paths do not traverse exactly the same points in space-time (Figure 1) and thus the two  
321 time series are not simply offset copies of each other. If the screen thickness is small, the peak  
322 correlation will be only slightly smaller than unity (i.e., the practical case for the 2001 DOY 149  
323 data). The decorrelation from unity can be used to estimate screen thickness. We simulated  
324 Kolmogorov turbulence [Woo & Armstrong 1979] in uniformly-weighted screens of varying  
325 thickness taking into account the differences in the ray paths of the up- and downlinks to produce  
326 synthetic Doppler time series. The simulated up- and downlink were then processed through the  
327 same software used to analyze the real data and the average peak correlation was determined  
328 over a simulated “tracking pass” of  $\approx 50000$  seconds (a little longer than a typical real tracking  
329 pass). The results are shown in Figure A2. (In the simulations, layers were added in 0.001 AU  
330 steps to the previous screen, so the points in Figure A2 are not statistically independent of each  
331 other.) The interval  $\approx 2210$ -2320 on 2001 DOY 149 has peak correlation  $> 0.97$ . Although this  
332 simulation approach is model-dependent (Kolmogorov turbulence, uniformly weighted screen),  
333 comparison with Figure A2 suggests the real data arise from a region having full-width thickness  
334  $\approx 0.02$  AU or smaller.

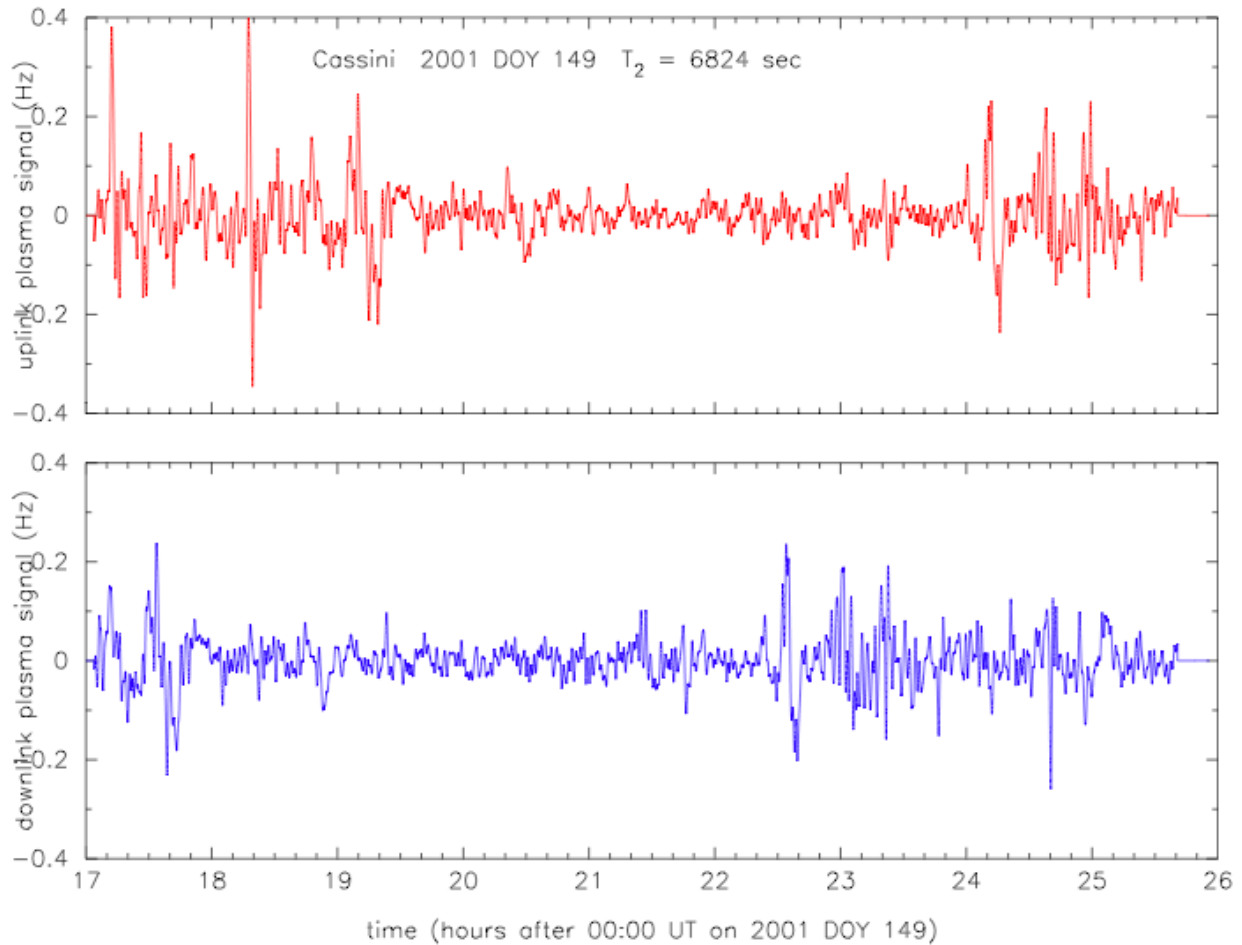


335

336 **Figure 1.** Transfer function of plasma fluctuations to one- and two-way phase/Doppler  
 337 scintillation allows localization of plasma blobs along the line-of-sight. Upper plot is a space-  
 338 time diagram (space vertically, time horizontally). The ground station and the spacecraft are  
 339 continuously exchanging microwave signals, some of which are shown as dashed lines. If the  
 340 signals pass through a well-localized plasma blob (indicated by the cross-hatched circular area)  
 341 the phase is perturbed. This perturbation is observed on both the uplink and downlink signals  
 342 and on the “two-way” (coherently transponded) Doppler. The two-way,  $y_2(t)$ , and the one-way  
 343 plasma-contribution Doppler time series,  $y_{up}(t)$  and  $y_{dn}(t)$ , are shown in the lower plot. The  
 344 phase perturbation is seen initially on the downlink, and – in the two-way Doppler -- latter when  
 345 the perturbation on the uplink is phase-coherently re-transmitted back to the ground. The effect  
 346 in  $y_2(t)$  is two positively-correlated features in the time series, separated in time by  $T_2 - 2x/c$ ,  
 347 where  $T_2$  is the two-way light time and  $x$  is the distance of the blob from the earth. The one-way  
 348 up and down Doppler time series detect the blob once each, but also separated by  $T_2 - 2x/c$ .  
 349 Crosscorrelation or windowed matched filtering between pairs of Doppler time series allows  
 350 estimates of the time delay, localizing the blob.

351

352

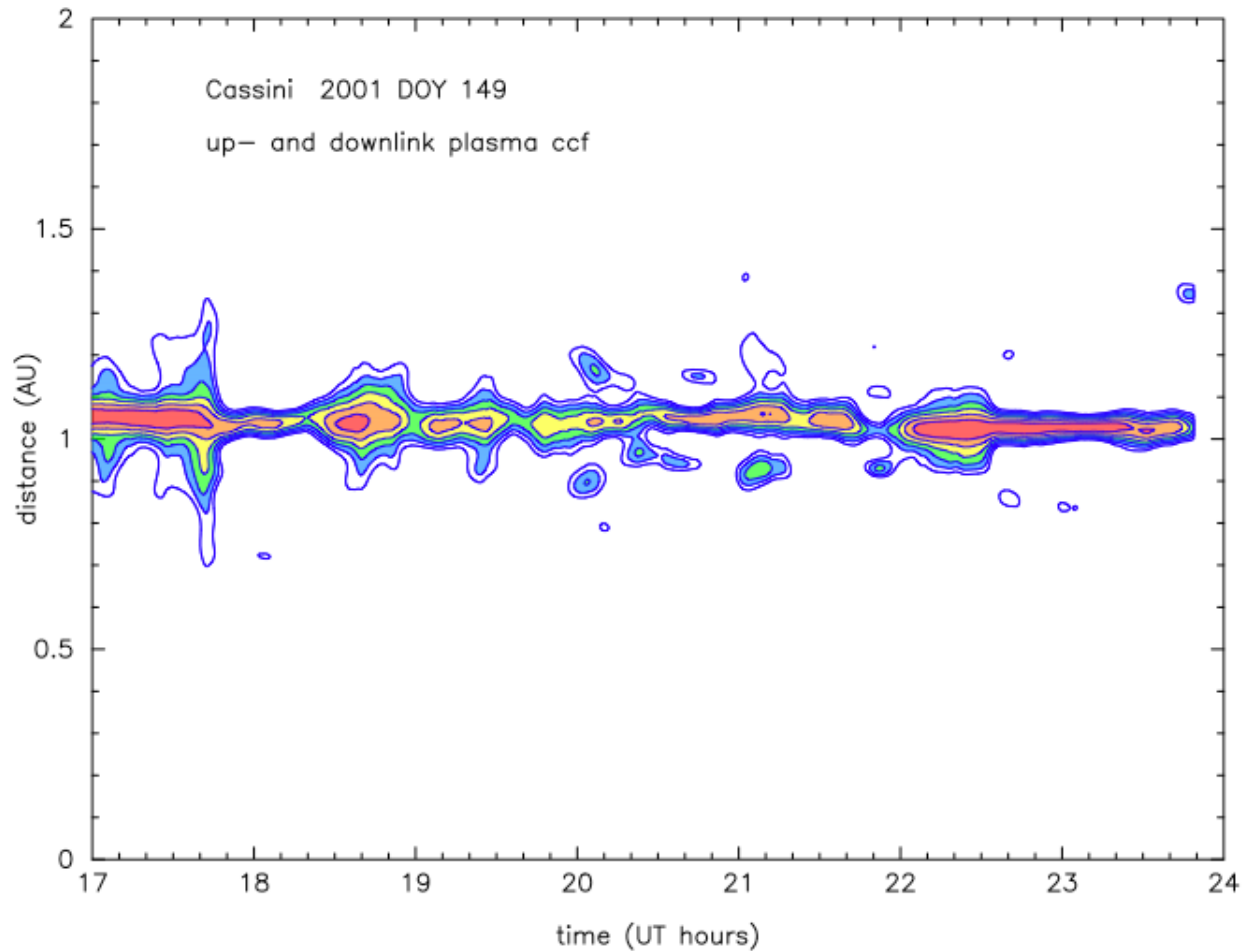


353

354

355 **Figure 2.** Time series of the plasma contribution to the X-band up- and down links,  $y_{up}(t)$  and  
 356  $y_{dn}(t)$ , for DSS25 Cassini track on 2001 DOY 149 = 2001 May 29. The two-way light time  $T_2$   
 357 was  $\approx 6824$  seconds. Several large amplitude features in the downlink time series (at e.g. about  
 358 1730 UT, 2230 UT, 2300 UT) have clear “echoes” in the uplink time series with time difference  
 359  $\sim T_2 - 2 \cdot 1.028$  AU/c. Figure 3 shows the windowed cross correlation (see text) of these two time  
 360 series, quantifying the space-time location of the plasma causing the Doppler variability.

361



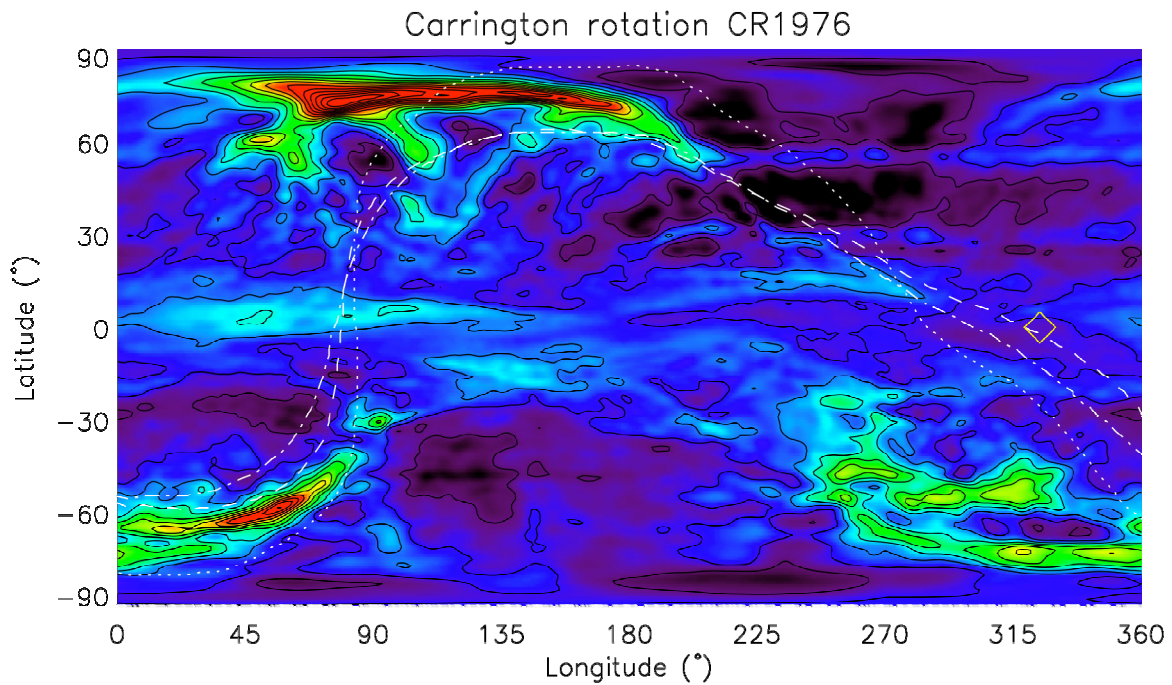
362

363

364 **Figure 3.** Space-time cross correlation function of the 2001 DOY 149 plasma up- and downlink  
 365 time series plotted in Figure 2. Y-axis is the distance from the Earth; x-axis is downlink received  
 366 time. Contours of cross correlation value are plotted between 0.9 and 0.4, in 0.1 increments.  
 367 Correlations  $> 0.9$  are shaded red, those between 0.8 and 0.9 in orange, and so forth. The  
 368 accuracy of the range determination and bounds to the thickness of the region contributing the  
 369 scintillation are discussed in the text.

370

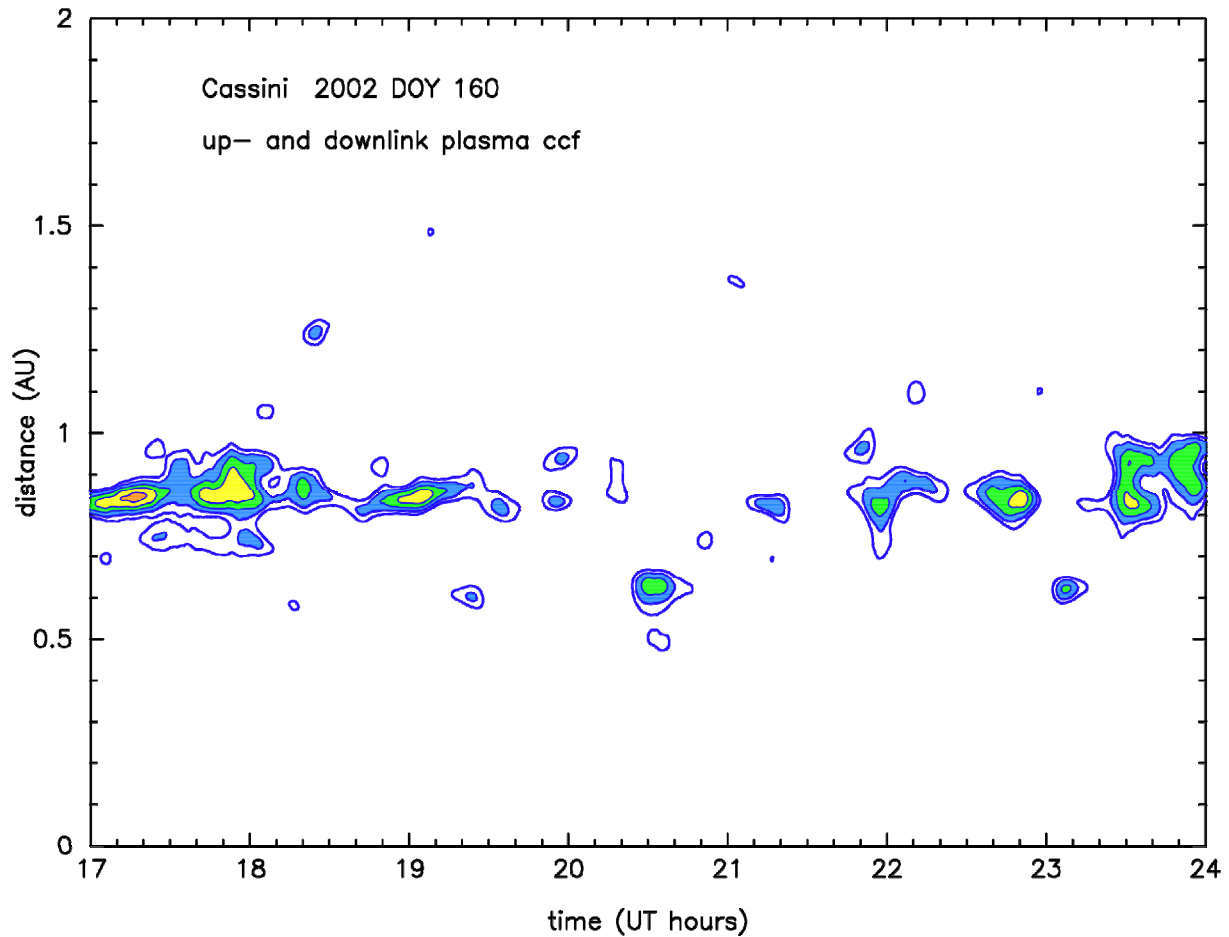
371



373

374

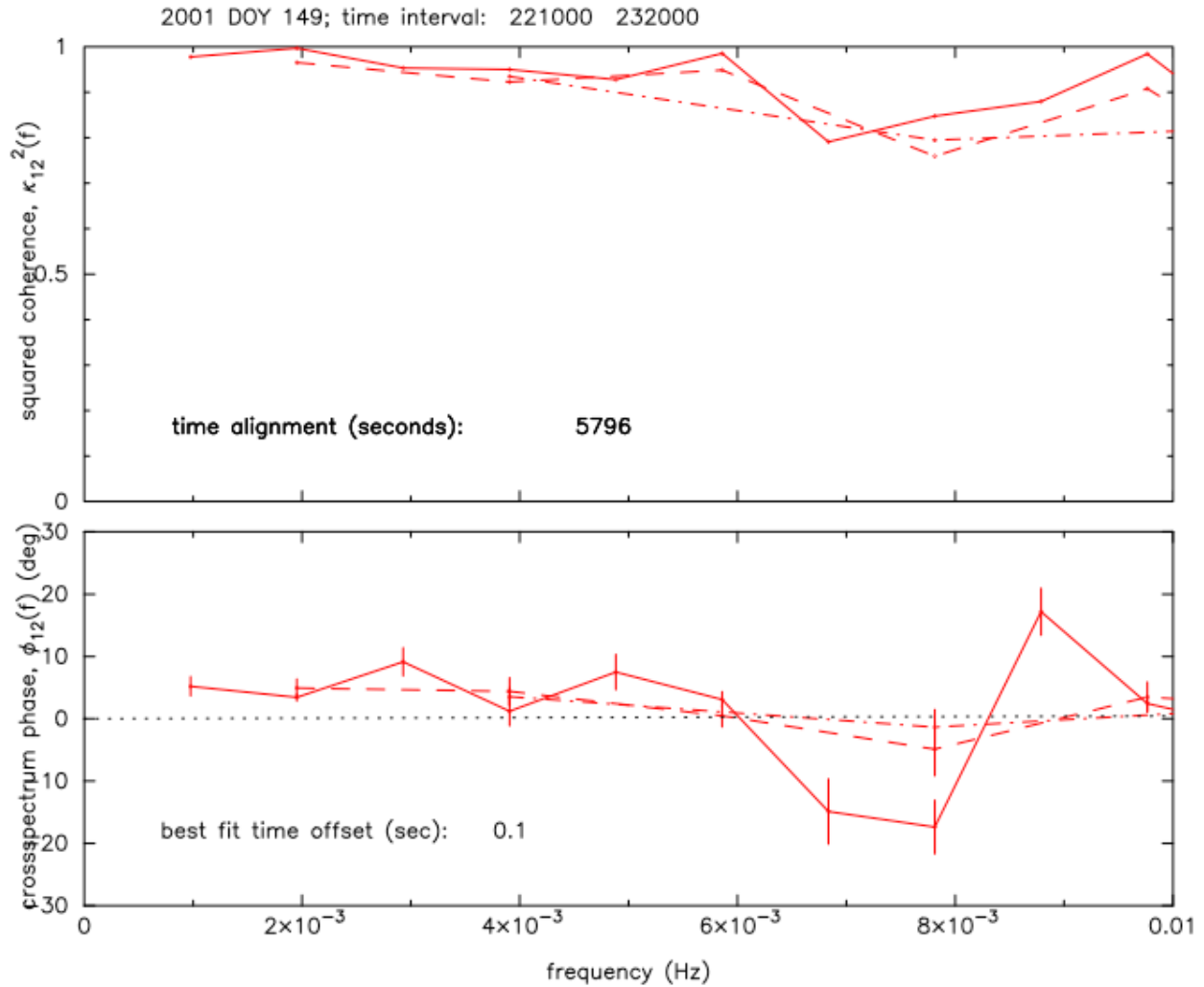
375 **Figure 4.** Map of coronal density structure at a height of 4 solar radii for Carrington Rotation  
 376 1976, calculated using a solar rotational tomography technique from ~2 weeks of  
 377 LASCO/SOHO C2 coronagraph observations. Red is high density, black is low. The x-axis  
 378 refers to Carrington longitude (CRL), the y-axis to solar latitude. The point along the earth-  
 379 Cassini line of sight closest to the sun is shown as a diamond at CRL 324 degrees on the map.  
 380 The three dotted and dashed lines are the position of the heliospheric current sheet (HCS),  
 381 calculated using a potential field source surface (PFSS) extrapolation of photospheric magnetic  
 382 field observations made by the Wilcox Solar Observatory. (The three lines give different  
 383 positions of the HCS when different boundary conditions are applied. See main text.)  
 384



385

386 **Figure 5.** As Figure 3, but for 2002 DOY 160 = 2002 June 9. The sun-earth-spacecraft angle  
 387 was about 9.5 degrees and the two-way light time was about 8365 seconds. Correlation levels in  
 388 general lower than those in Figure 3. At the start of the track a scattering region nearer to the  
 389 earth than the raypath closest approach point ( $\approx 1\text{AU} \cos(9.5 \text{ degrees}) = 0.986 \text{ AU}$ ) is indicated.  
 390 In mid-track the correlation is particularly low, indicative of extended, rather than localized,  
 391 scattering.



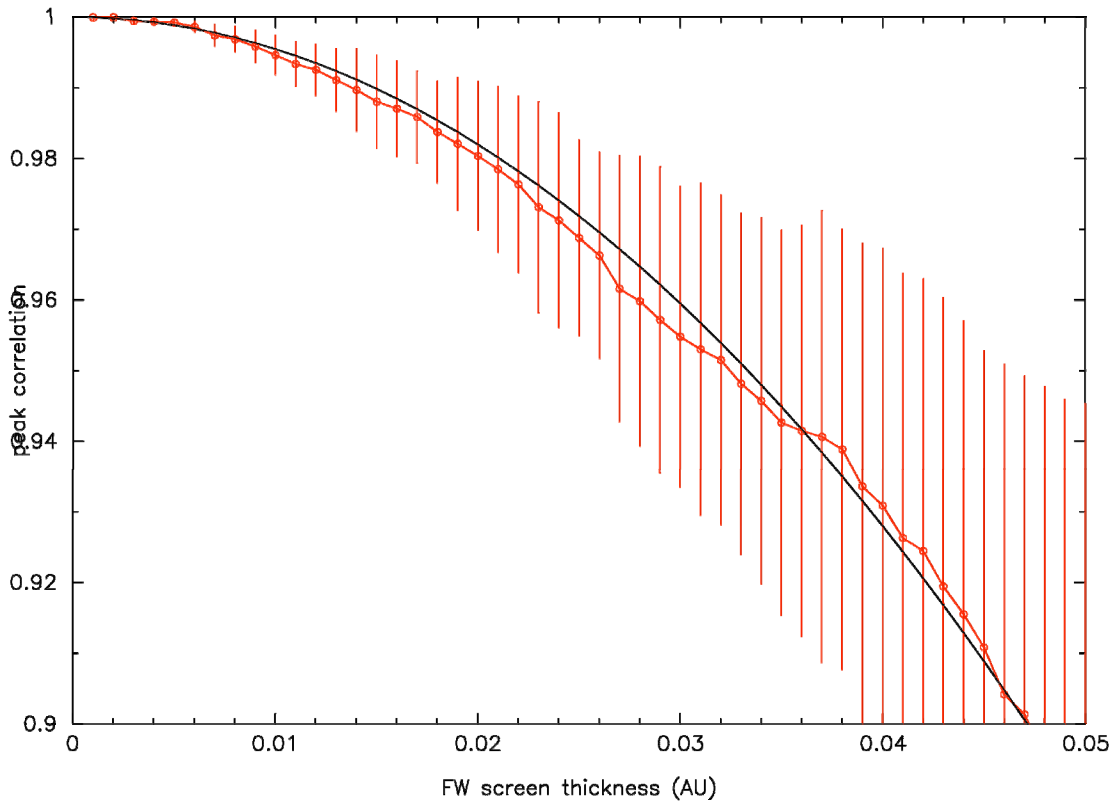


392

393 **Figure A1.** Smoothed squared coherence and smoothed cross-spectral phase for the up- and  
 394 downlink plasma contributions for time interval 2001 DOY 149 2210-2320 UT. The data have  
 395 been pre-aligned by 5796 seconds and analyzed with resolution bandwidths of 1/1024 Hz (solid  
 396 line), 1/512 Hz (dashed line), and 1/256 Hz (dot-dash lines). Uncertainties shown for the cross  
 397 spectral phase are formal  $\pm 3$  sigma, based on the numbers of degrees of freedom in the  
 398 estimates and on the squared-coherency at each frequency [*Jenkins and Watts 1969*, equation  
 399 9.2.21]. The non-zero slope in the phase spectrum gives a refined estimate for the lag giving best  
 400 correlation between the up- and downlink plasma time series: 5796.1 seconds. The uncertainty  
 401 in the slope gives an uncertainty in this time offset and hence an uncertainty in the distance to the  
 402 screen (see Appendix).

403

404



405  
 406 **Figure A2.** Peak correlation value versus full-width screen thickness from simulations of  
 407 Kolmogorov-spectrum turbulence. Simulated data were produced from uniformly weighted  
 408 layers over the indicated full-width thickness with the "near" edge of the turbulence in the  
 409 simulation at 1 AU. Red points are peak correlation and standard deviation for simulations of  
 410 length slightly longer than one actual tracking pass, processed though the same software used in  
 411 the analysis of the Figure 3 and 5 data. Black line is a smooth curve, not a fit. For screen  
 412 thickness small compared with the time constant of the low pass filtering, cross-correlation  
 413 function width is set by the low-pass filtering and its decorrelation from unity can be used to  
 414 estimate screen thickness.  
 415

416 **References**

- 417
- 418 Altschuler, M. D. & Newkirk, G. (1969) "Magnetic Fields and the Structure of the Solar  
419 Corona. I: Methods of Calculating Coronal Fields" *Solar Physics*, **9**, 131-149  
420 10.1007/BF00145734
- 421
- 422 Armstrong, J.W. (2006) "Low-Frequency Gravitational Wave Searches Using Spacecraft  
423 Doppler Tracking", *Living Rev. Relativity*, **9**, 1 [Online Article]: cited 4 May 2009,  
424 <http://www.livingreviews.org/lrr-2006-1>
- 425
- 426 Asmar, S.W., Armstrong, J.W., Iess, L., & Tortora, P. (2005) "Spacecraft Doppler Tracking:  
427 Noise Budget and Achievable Accuracy in Precision Radio Science Observations", *Radio*  
428 *Science* **40**, RS2001 10.1029/2004RS003101
- 429
- 430 Bertotti, B., Iess, L., & Tortora, P. (2003) "A Test of General Relativity Using Radio Links  
431 with the Cassini Spacecraft", *Nature*, **425**, 374-376.
- 432
- 433 Bracewell, R. (1965) *The Fourier Transform and Its Applications* (McGraw-Hill: New York).
- 434
- 435 Brueckner, G. E., Howard, R. A., Koomen, M. J., Korendyke, C. M., Michels, D. J., Moses, J.  
436 D., Socker, G. G., Dere, K. P., Lamy, P. L., Llebaria, A., Bout, M. V., Schwenn, R.,  
437 Simnett, G. M. Benford, D. K., & Eyles, C. J. (1995) "The Large Angle Spectroscopic  
438 Coronagraph (LASCO)", *Solar Physics*, **162**, 357-402.
- 439
- 440 Estabrook, F.B. (1978) "Gravitational Wave Detection With the Solar Probe. II. The Doppler  
441 Tracking Method" in *A Close-Up of the Sun* (JPL Publication 78-70), September 1, 1978, pp.  
442 441-449.
- 443
- 444 Estabrook, F.B. & Wahlquist, H.D. (1975) "Response of Doppler Spacecraft Tracking to  
445 Gravitational Radiation" *Gen. Rel. Grav.*, **6**, 439-447.
- 446
- 447 Iess, L., Anderson, J. D., Asmar, S. W., Barbini, E., Bertotti, B., Fleischman, D. U., Gatti, M.  
448 S., Goltz, G. L., Herrera, R. G., Lau, E. & Oudrhiri, K. (2003) "The Cassini Solar  
449 Conjunctions Experiment: A New Test of General Relativity", in *Proceedings of the IEEE*  
450 *Aerospace Conference 2003*, Big Sky, MT, March 8-15, 2003, IEEE Conference  
451 Proceedings, 1-211-223 Institute of Electrical and Electronic Engineers, Piscataway, USA,  
452 2003)
- 453
- 454 Jenkins, G.M. & Watts, D.G. (1969) *Spectral Analysis and Its Applications* (Holden-Day: San  
455 Francisco).
- 456
- 457 Kliore, A.J., Anderson, J. D., Armstrong, J. W., Asmar, S. W., Hamilton, C. L., Rappaport, N. J.,  
458 Wahlquist, H. D., Anbrosini, R., Flasar, F. M., French, R. G., Iess, L., Marouf, E. A. & Nagy,  
459 A. F. (2004) "Cassini Radio Science", *Space Science Reviews* **115**, 1-70.
- 460

461 Morgan, H. & Habbal, S. R. (2007) "An Empirical 3D Model of the Large-Scale Coronal  
462 Structure Based on the Distribution of H $\alpha$  Filaments on the Solar Disk", *Astron. Astrophys.*,  
463 **464**, 357-365 10.1051/0004-6361:20066482  
464

465 Morgan, H., Habbal, S. R., & Lugaz, N. (2009) "Mapping the Structure of the Corona Using  
466 Fourier Backprojection Tomography", *Ap. J.*, **690**, 1119-1129 10.1088/0004-  
467 637X/690/2/1119  
468

469 Shatten, K. H., Wilcox, J. M., & Ness, N. F. (1969) "A Model of Interplanetary and Coronal  
470 Magnetic Fields", *Solar Physics*, **6**, 442-455 10.1007/BF00146478  
471

472 Smith, E. (2001) "The Heliospheric Current Sheet", *JGR*, **106** (A8), 15819-15831  
473

474 Tortora, P., Iess, L., & Ekelund, J. E. "Accurate Navigation of Deep Space Probes using  
475 Multifrequency Links: the Cassini Breakthrough During Solar Conjunction Experiments",  
476 The World Space Congress, October 10-19, 2002, Houston, USA  
477

478 Tortora, P., Iess, L., & Herrera, R. G. "The Cassini Multifrequency Link Performance During  
479 2002 Solar Conjunction", *Proceedings of the IEEE Aerospace Conference*, March 8-15,  
480 2003, Big Sky, Montana, USA, Vol. 3, 1465-1473  
481

482 Tortora, P., Iess, L., Bordi, J.J., Ekelund, J.E., & Roth, D.C. (2004) "Precise Cassini Navigation  
483 During Solar Conjunctions through Multifrequency Plasma Calibrations", *Journal of*  
484 *Guidance, Control and Dynamics*, **27**, 251-257.  
485

486 Tyler, G. L., G. Balmino, D. P. Hinson, W. L. Sjogren, D. E. Smith, R. A. Simpson, S. W.  
487 Asmar, P. Priest, & J. D. Twicken (2001) "Radio Science Observations with Mars Global  
488 Surveyor: Orbit Insertion Through One Mars Year in Mapping Orbit," *Journal of*  
489 *Geophysical Research - Planets* 106(E10), 23327-23348.  
490

491 Vessot, R.F.C. & M.W. Levine (1978) "A Time-Correlated Four-Link Doppler Tracking  
492 System" in *A Close-Up of the Sun* (JPL Publication 78-70), September 1, 1978, pp. 457-497.  
493

494 Wang, Y.-M. & Sheeley, N. R. (1992) "On Potential Field Models of the Solar Corona" *Ap. J.*,  
495 **392**, 310-319 10.1086/171430  
496

497 Winterhalter, D., Smith, E. J., Burton, M. E., Murphy, N., & McComas, D. J. (1994) "The  
498 Heliospheric Plasma Sheet" *JGR*, **99** (A4), 6667-6680  
499

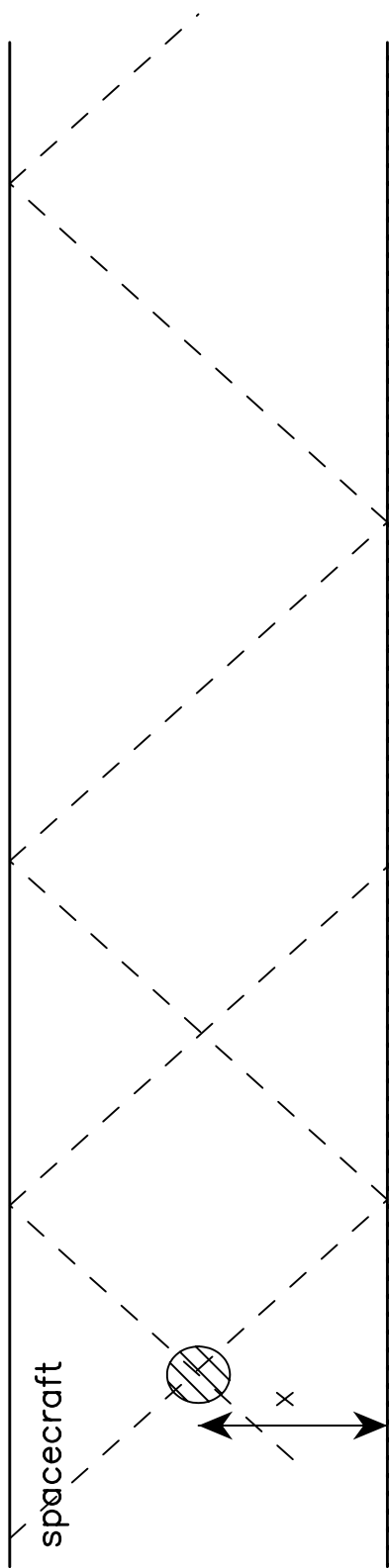
500 Woo, R. (2007) "Space Weather and Deep Space Communications" *Space Weather*, **5**, S09004,  
501 doi:10.1029/2006SW000307  
502

503 Woo, R. & Armstrong, J., W. (1979) "Spacecraft Radio Scattering Observations of the Power  
504 Spectrum of Electron Density Fluctuations in the Solar Wind", *JGR*, **84**, 7288-7296.  
505

506 Woo, Richard, Armstrong J.W., & Gazis, P. (1995) "Doppler Scintillation Measurements of the  
507 Heliospheric Current Sheet and Coronal Streamers Close to the Sun" *Space Science Reviews*,  
508 **72**, 223-228.

509

510 Zhou, X.-Y., Smith, E. J., Winterhalter, D., McComas, D. J., Skoug, R. M., Goldstein, B. E. &  
511 Smith, C. W. (2005) "Morphology and Evolution of the Heliospheric Current and Plasma  
512 Sheets From 1 to 5 AU" in *Proc. Solar Wind 11-SOHO 16 "Connecting Sun and*  
513 *Heliosphere"*, Whistler, Canada 12-17 June 2005 (ESA SP-592, September 2005).



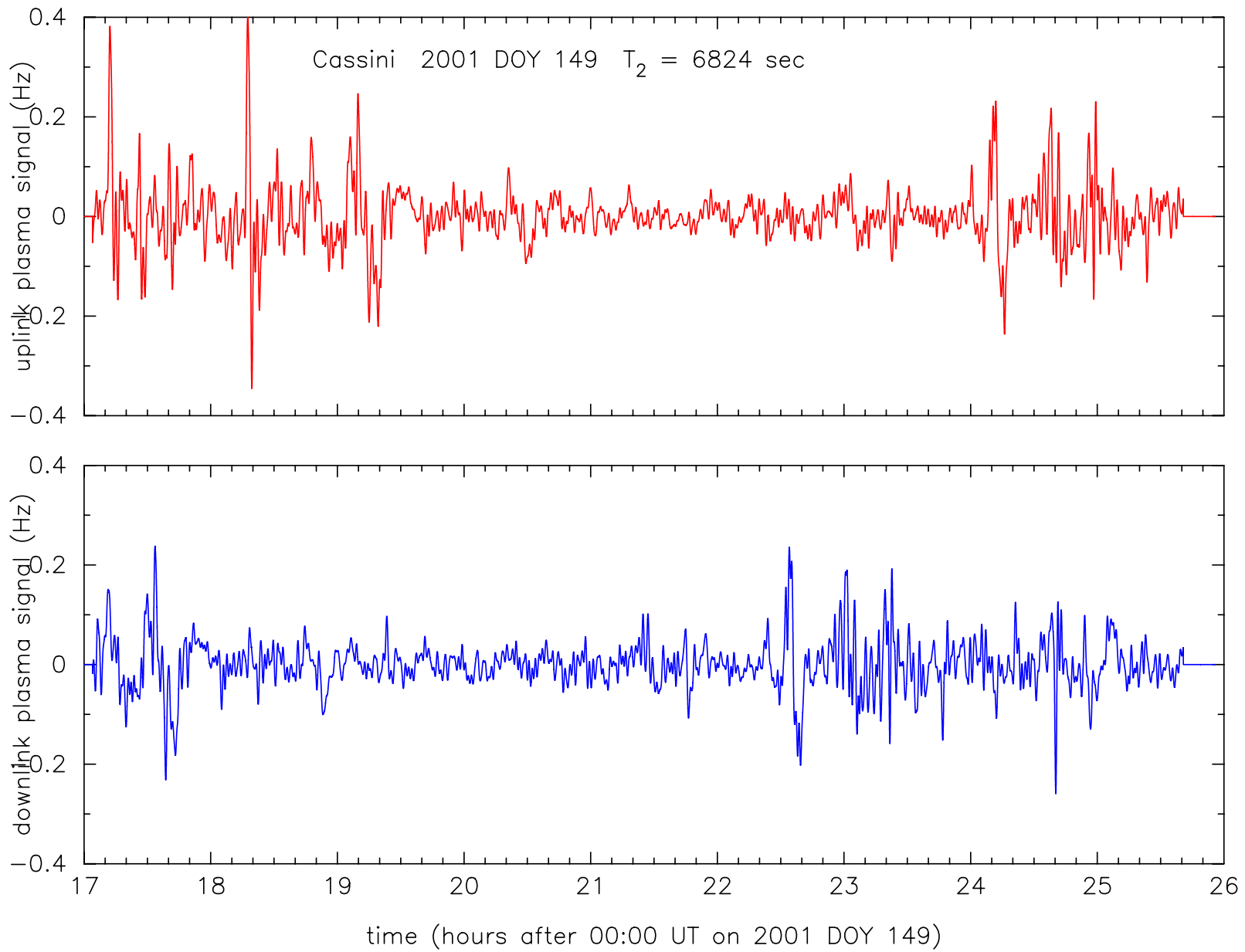
$T_2$

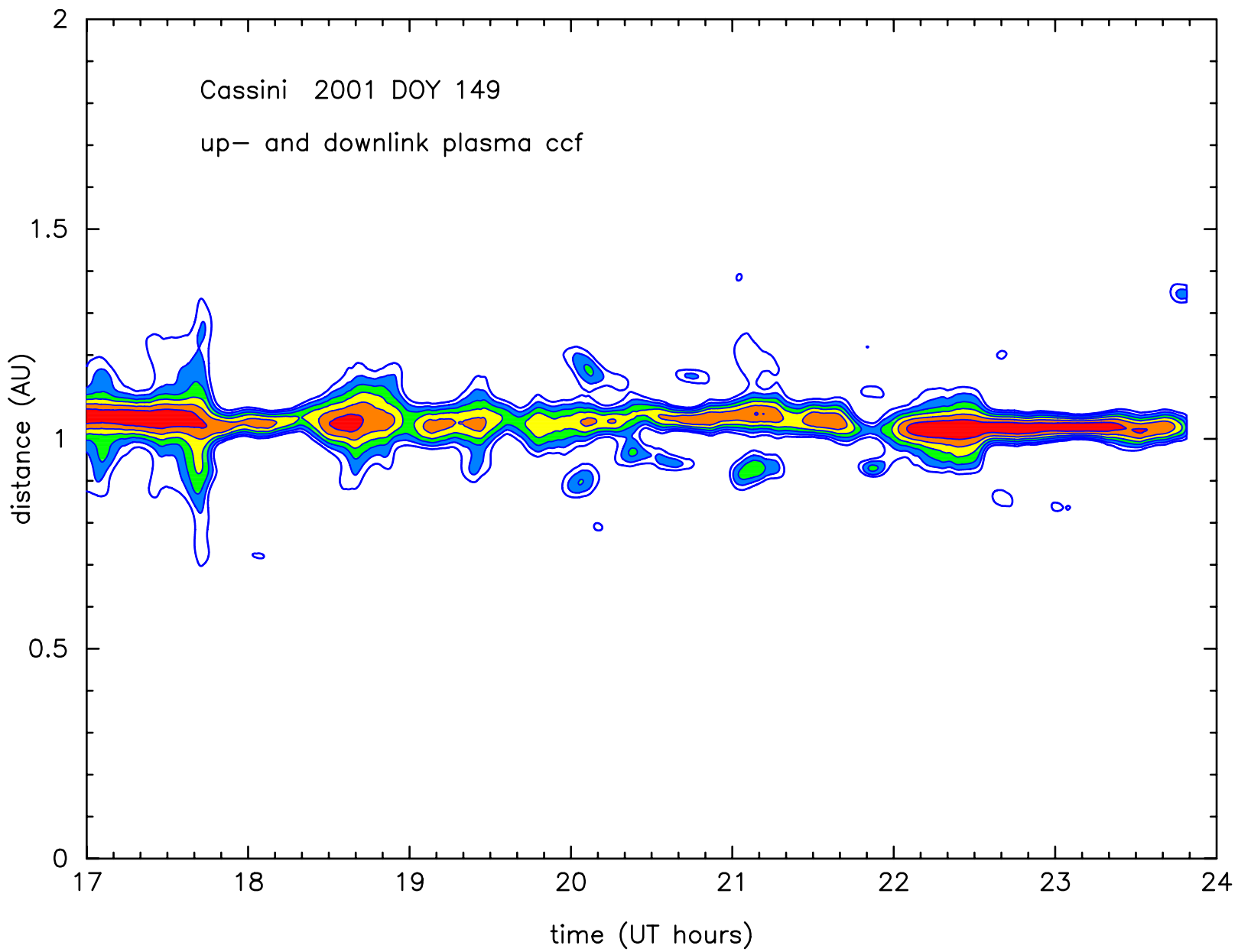
$y_2(t)$

$T_2 - 2x/c$

$y_{dn}(t)$

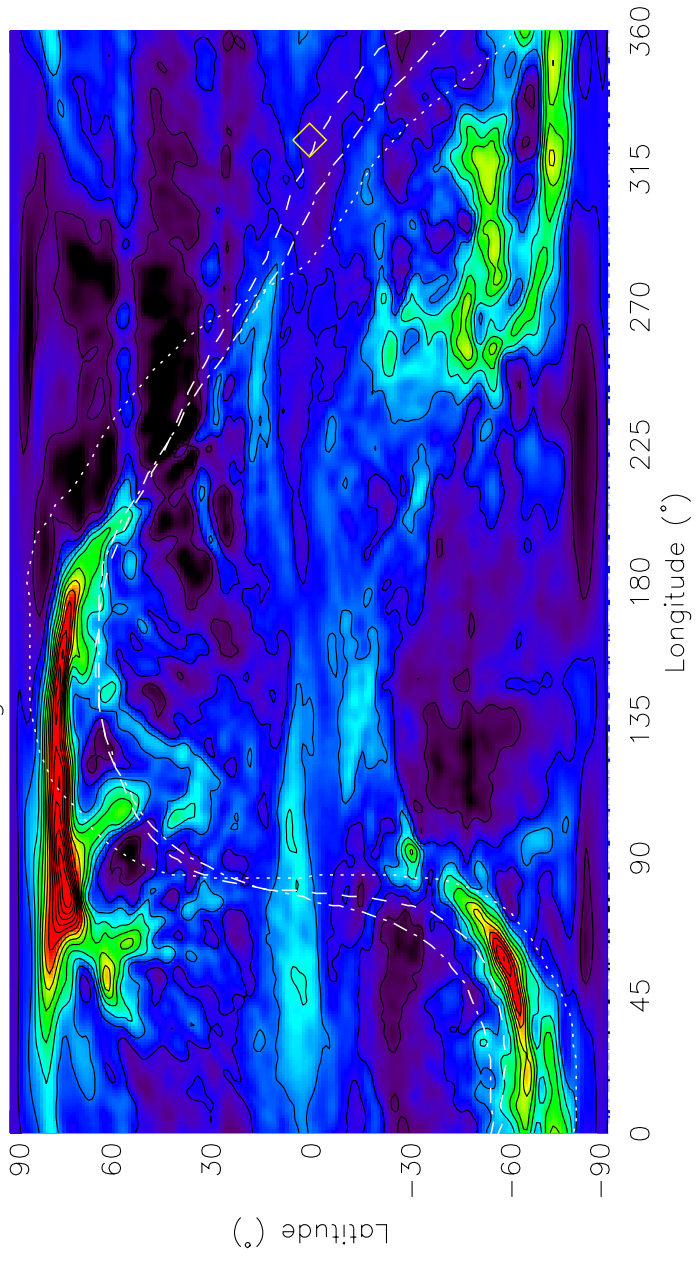
$y_{up}(t)$

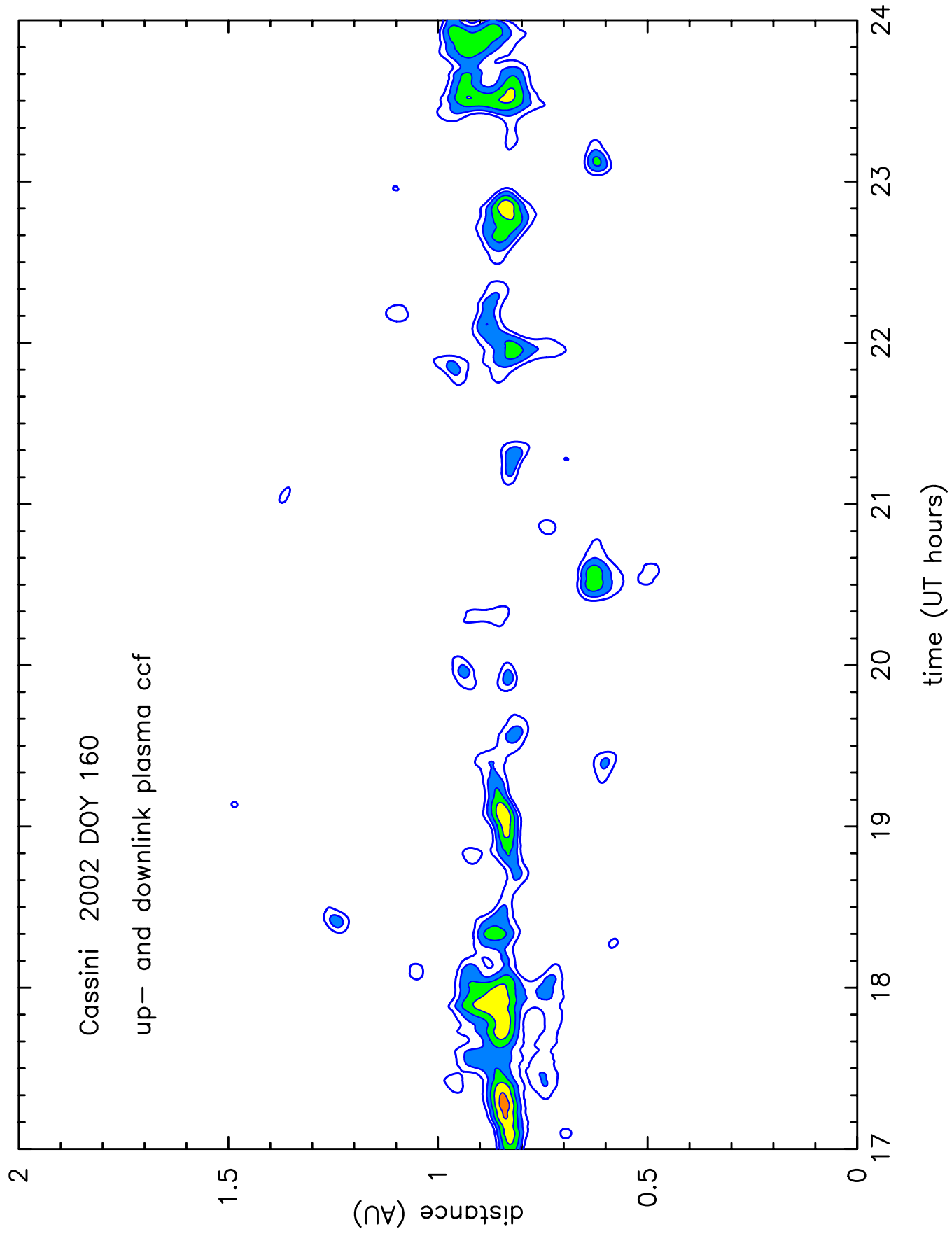






Carrington rotation CR1976





2001 DOY 149; time interval: 221000 232000

